

Fiber-bundle-based gradient light interference endoscopic microscopy

Jingyi Wang¹, Chenfei Hu², Wu You¹, Yuheng Jiao¹,
Yanhong Zhu³, Xiaojun Liu¹, Xiangqian Jiang^{1,4}, Wenlong Lu^{1,5*}

¹State Key Laboratory of Digital Manufacturing Equipment and Technology, School of Mechanical Science and Engineering, Huazhong University of Science and Technology, Wuhan, 430074, PR China.

² Applied Materials, Inc., Santa Clara, 95054, USA.

³National Engineering Research Center for Nanomedicine, College of Life Science and Technology, Huazhong University of Science and Technology, Wuhan, 430074, PR China.

⁴EPSRC Future Metrology Hub, EPSRC Future Metrology Hub, Huddersfield, HD1 3DH, UK.

⁵Shenzhen-HUST Research Institute, Huazhong University of Science and Technology, Shenzhen, 518057, PR China.

*Corresponding author(s). E-mail(s): hustwenlong@mail.hust.edu.cn;

Abstract

The flexible endoscope is a minimally invasive tool in clinical settings, but most of them only provide qualitative amplitude information and require puncture biopsy or exogenous staining for diagnosis. These limitations restrict their use for rapid investigation. Here, we developed a fiber-bundle-based gradient light interference endoscopic microscopy (FGLIM) in reflection geometry for quantitative phase imaging of unlabeled thick samples. FGLIM provides the phase information by wavefront modulation using chessboard grating and phase-shifting. FGLIM system features high lateral and axial resolutions of 1.2 and 8.3 μm , respectively, with a probe diameter of 2.5 mm. By testing pathologic slices and thick opaque mammalian tissue ex vivo, FGLIM identifies normal and tumor glandular structures, secreta, and tomographic skin layers. With the potential for direct morphological and phase measurement, high resolution, and thin fiber tip, the label-free FGLIM could be an attractive tool for various clinical applications.

1 Introduction

Flexible endoscope is a significant clinical tool for diagnosis and therapeutics [1–3], due to great surgical freedom, minimally invasion and high imaging quality. As conventional digital endoscope only provides amplitude imaging of the surface, novel techniques like confocal endoscopy, multiphoton endoscopy and optical coherence tomography endoscopy have been developed for depth sectioning recently. Multiphoton endoscopy and confocal laser endoscopy provide cell-level resolution images with specific information revealed by fluorescent tags [4–7]. However, aside from intrinsic fluorescence imaging, they need the tagging procedure and suffer from phototoxicity and photobleaching. Optical coherence tomography provides label-free images with a deep depth of imaging, but often needs lateral scanning modules to get *en face* images and only provides back scattering amplitude information [8, 9].

Phase is an important endogenous contrast information, which indicates optical path length shifts resulting from variations in the refractive index of a sample. Quantitative phase imaging (QPI) is a fascinating technique in biomedicine that provides sub-cellular structural information and achieves phase mapping of biophysical parameters with nanometer-scale sensitivity [10]. This technique has numerous biomedical applications, including live cell imaging, cancer diagnosis, hematology, and pathology [10–15]. However, most QPI techniques use trans-illumination and cannot penetrate deep into thick and opaque specimens, limiting their potential applications in clinical settings. Recently, several reflection-mode QPI techniques with optical sectioning ability have emerged, including confocal reflectance interferometric microscopy [16], reflection phase microscopy [17], dynamic speckle-field interferometric microscopy [18] and epi-illumination gradient light microscopy [19]. These techniques can quantify fluctuations of cells and nuclei at the nanometer scale or show potential for thick specimens imaging, but they have not been developed into endoscopes for broader clinical applications.

Efforts have been devoted to endoscopic QPI systems, such as rigid endoscopic diffraction phase microscopy and flexible holographic endoscopes, which have their own advantages and limitations. Rigid endoscopic diffraction phase microscopy [20] enables real time single shot imaging, but it is slow in operation and lacks accessibility to certain tissue types, such as sinuous areas. In contrast, flexible holographic endoscopes [21–23] achieves high resolution images with ultra thin lensless fiber tip. Specifically, the holographic endoscope [23] is based on Mach-Zehnder interferometry and needs scanning mechanism for illumination and calibrating the reflection matrix iteratively for fiber phase retardation compensation, which compromises temporal stability and throughput. These holographic endoscopes have been validated on thin slices and cells at present. Due to the interference scheme, holographic endoscopes require a coherent light source, such as lasers, which suffer from the speckle effect. The quantitative oblique back illumination fiber endoscope [24–26], a speckle-free system using LED illumination, shows morphological differences between normal and tumor regions of thick brain tissue but lacks parameters of penetration depth and axial resolution. The fiber tip is 4mm thick and would be limited in narrow spaces, such as the nasal sinus. The phase reconstruction process is based on numerical modeling and thus becomes computationally expensive.

In this paper, we develop a fiber-bundle-based gradient light interference endoscopic microscopy (FGLIM), which works in reflection geometry to achieve high-resolution imaging of biological samples. FGLIM has a 2.5 mm thick tip and measures phase directly without complicated modeling and reconstruction. We use an amplitude-type SLM to generate chessboard gratings in the Fourier plane, which enables lateral shearing and phase shifting. By utilizing a phase retrieval algorithm, FGLIM obtains orthogonal phase gradients simultaneously and suppresses the multiple scattering background and the phase delay introduced by the fiber bundle. Furthermore, a partially coherent light source, combined with annular illumination, allows for optical sectioning ability. The use of checkerboard Fourier modulation in common path structure preserves spatial resolution while also enabling imaging speeds twice as fast as those achieved with sinusoidal gratings [27, 28]. By measuring microspheres and patterned structures on a scattering substrate, FGLIM demonstrates high quality phase imaging capability, with transverse and axial resolution of 1.2 and 8.3 μm , respectively. Furthermore, by measuring histological slides, and mammalian tissue *ex vivo*, the phase images measured by FGLIM can clearly identify normal and tumor glandular structures, secretory, stroma and different skin layers. We also validate the depth of penetration of 180 μm with tomographic images of the thick opaque mammalian tissue. The non-destructive tomographic investigation ability, approximate microscopic resolution, and potential diagnosis information provided by FGLIM might make it an interesting for clinical applications.

2 Results

2.1 FGLIM System Design

The FGLIM system, illustrated in Fig.1, consists of two key components: endoscopic optics and microscopic optics. Endoscopic optics are utilized for illumination and wavefront transmission, whereas microscopic optics are employed for imaging and wavefront modulation. To achieve illumination, a 780nm LED is coupled into the light guide and illumination fibers. As depicted in Fig.1 (a), the illumination fibers are positioned surrounding the fiber bundle to create a ring illumination pattern. The outer diameter of the probe distal end is approximately 2.5 mm. In the imaging geometry, light reflected from the sample is collected by a gradient refractive index (GRIN, 2.6X) lens and transmitted through the fiber bundle to the front focal plane of the objective, as illustrated in Fig.1 (b). The GRIN lens, along with the objective (10X, NA=0.4) and tube lens, magnifies the sample field by a factor of 26, resulting in sufficient spatial sampling for high-resolution images. The FGLIM system employs a grating to split the wavefront into four orthogonal replicas with phase shifts, allowing for self-interference and generation of interferograms. In order to perform chessboard gratings, an amplitude-type spatial light modulator (SLM) is employed in the Fourier plane of a 4f system (lens L1 and lens L2), as shown in Fig.1 (c). The shear distance, which is controlled by modifying the grating period on the SLM, is below the diffraction limit. The interferograms of the differentiated light are then captured by a CMOS, with a field of view of approximately 250 μm in diameter. This self-interference mechanism ensures high temporal stability.

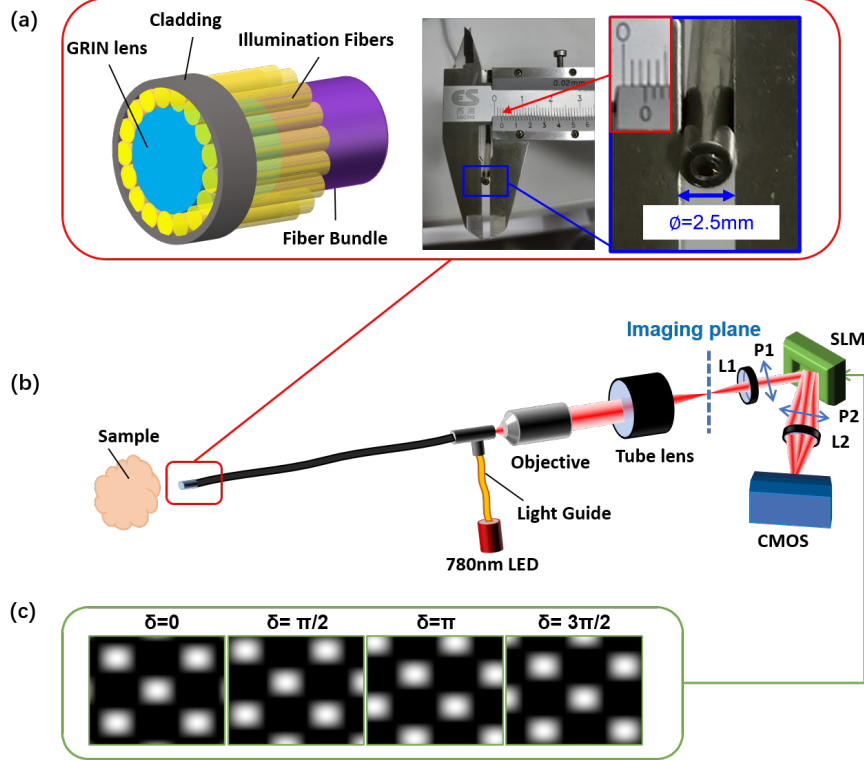


Fig. 1 Schematic representation of the system. (a) View of the probe distal end. The GRIN lens acts as miniature objective and the fiber bundle transfers back focal plane images to the proximal end of the tip. The illumination fibers surround the GRIN lens and fiber bundle to form ring illumination. The total diameter of the cladding protected fiber tip is 2.5 mm. (b) LED light is transmitted through the light guide for illumination, while the objective lens, accompanied by the tube lens, collects images that are transferred by the fiber bundle. L1 and L2 are lenses in a 4f system, and P1 and P2 are linear polarizers. The polarization of P1 is parallel to the liquid crystal axis, and perpendicular to that of P2, to help SLM achieve amplitude modulation. At the Fourier plane, the SLM generates gratings, as shown in (c), which introduces phase shifting and self-interference for quantitative phase imaging. The detailed information is described in Methods. (c) Four diffraction patterns are displayed on the SLM for phase shifting and wavefront shearing.

2.2 Image formation and signal processing

To investigate the photon propagation for FGLIM setup, we perform Monte Carlo simulation with PyXOpto [29–31]. To ensure sufficient illumination area while minimizing the probe tip size, we selected an illumination fiber with a higher numerical aperture (NA) and a smaller diameter compared to the detection fiber. The simulation details are described in Methods. In Fig.2 (a), we simulate the various layers of the thick tissue using scattering parameters reported in the literature [32, 33]. The simulation traced the scattering progress of light photons emitted from the illumination fiber and traveling to the detector fiber through the sample. The resulting image in Fig.2 (b) shows the sampling volume and provides a color bar with the product value of the terminal photon packet weight and the pathlength in the sampling volume

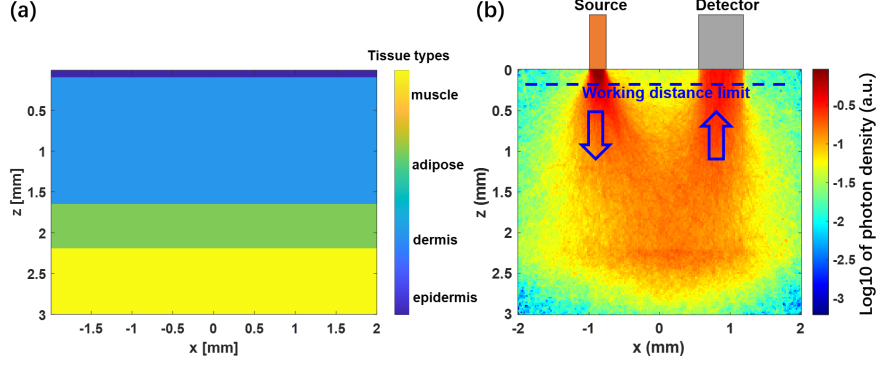


Fig. 2 Monte Carlo simulation for photon path through the skin tissue. (a) Illustration of the different skin layers: 0.085 mm epidermis, 1.55 mm dermis, 0.55 mm adipose and 0.815 mm muscle. (b) The sampling volume is summed along the y axis, which indicates the multiple scattering effect of thick sample turns epi-illumination into virtual transmissive illumination. The working distance limit of the miniature objective is 180 μm in the air.

accumulator. Monte Carlo simulations demonstrate that illumination fibers in reflection geometry provide virtual trans-illumination by utilizing the multiple scattering properties of the specimen.

To obtain a quantitative measurement of phase, it is necessary to eliminate the phase delay introduced by the fiber bundle. Previous studies have utilized a linear forward model, such as the transmission matrix [34–38], to describe the relationship between the original image and the image degraded by the fiber. The linear model is not designed to address individual variations caused by fiber curvature or vibration, but rather to provide a reliable solution for fiber characterization. In our system, we define the forward model as:

$$U(r_{\perp}) = A_{ij}(r_{\perp}) e^{i\varphi_{ij}(r_{\perp})} \cdot \left[U_0(r_{\perp}) e^{i\varphi(r_{\perp})} \right], \quad (1)$$

where r_{\perp} is spatial coordinate, U_0 is the original sample field, i and j are partially spatial coordinates at the fiber bundle facet, A_{ij} is the amplitude variation caused by fiber bundle and can be canceled in phase shifting algorithm, φ is the target phase, φ_{ij} is the phase delay introduced by fiber bundle, and U is the light field after fiber optics transmission. The SLM at the Fourier plane displays diffraction gratings to modulate the light field, according to

$$U'(k_{\perp}) = U(k_{\perp}) \cdot \left[\cos\left(k_x \cdot x_0 + \frac{\delta}{2}\right) \cdot \cos\left(k_y \cdot y_0 + \frac{\delta}{2}\right) + DC \right], \quad (2)$$

where $U(k_{\perp})$ is the Fourier transform part of $U(r_{\perp})$, k_x and k_y are x and y components of k_{\perp} , x_0 and y_0 are shear distances introduced by the grating, $\delta = 0, \frac{\pi}{2}, \pi, \frac{3\pi}{2}$ is the additional phase shifts introduced by SLM, DC is the 0th diffraction order caused by SLM that can be canceled with the four-step phase shifting algorithm. The intensity image on the CMOS is

$$I(r_{\perp}) = |U'(r_{\perp})|^2, \quad (3)$$

where $U'(r_\perp)$ is the inverse Fourier transform part of $U'(k_\perp)$. The amplitude of four diffracted waves is assumed to be uniform as the shear distance is smaller than the diffraction limit. With the four-step phase shifting algorithm, we can get the phase of the field $U(r_\perp)$:

$$\Delta\varphi' = \frac{I_4 - I_2}{I_1 - I_3} = \Delta\varphi_{ij} + \Delta\varphi. \quad (4)$$

To get a background image, we collect backscattered light from the objective table without a target specimen, but using white printing papers as the substrate. We assume that the fiber maintains the phase, thus the phase difference can be $\Delta\varphi'' = \Delta\varphi_{ij}$. We can decouple the phase difference of the sample from the fiber deteriorated image with $\Delta\varphi = \Delta\varphi' - \Delta\varphi''$, such that the sample phase φ is obtained via

$$\varphi = FT^{-1} \left[\frac{FT(\Delta\varphi) \cdot H^*}{H \cdot H^* + \varepsilon} \right], \quad (5)$$

with

$$H(k_\perp) = e^{2\pi i(x_0 \cdot k_x + y_0 \cdot k_y)} - 1, \quad (6)$$

where FT represents Fourier transform, ε is a regularization parameter to control the trade off between resolution enhancement and noise amplification [39], H^* is the complex conjugate of H .

3 Results

3.1 Imaging standard objects

For imaging experiments on standard or sliced histological objects, a fold of white printing paper, approximately 1 mm thick, is placed under the specimen as an opaque scattering substrate, such that multiple scattering tissue condition, as simulated in the Monte-Carlo in Section 2.2, is satisfied.

We investigated the phase sensitivity of the FGLIM system, which shows the ability to detect the lowest optical path length value from the noise floor [40]. The spatial-temporal noise level, measured to be 16 nm, highlights the nanoscale axial sensitivity of the optical path length that the system can achieve. This makes it possible to detect even subtle changes in the refractive index of biological samples with high precision. The measuring process is detailed in Supplementary Section 1.

To quantify the lateral and axial resolution of our system, we scanned 700 nm polystyrene beads placed on a glass slide with a step size of 1 μm axially. Figure 3 (a) shows planar and axially scanned images of a selected bead in the red box, with the sample-free background image subtracted. We analyzed the intensity from Fig. 3 (a) to obtain the point spread function (PSF) for resolution quantification. The lateral resolution of the system is limited by the sampling of the fiber bundle cores, which is equal to the single-core size divided by the magnitude of the gradient index (GRIN) lens. The full width at half maximum (FWHM) of the measured PSF function for lateral resolution is 1.2 μm , as shown in Fig. 3 (b), which is slightly larger than the theoretical value of $3 \mu\text{m} / 2.6 = 1.15 \mu\text{m}$. The axial resolution is measured to be 8.3 μm , as shown in Fig. 3 (c).

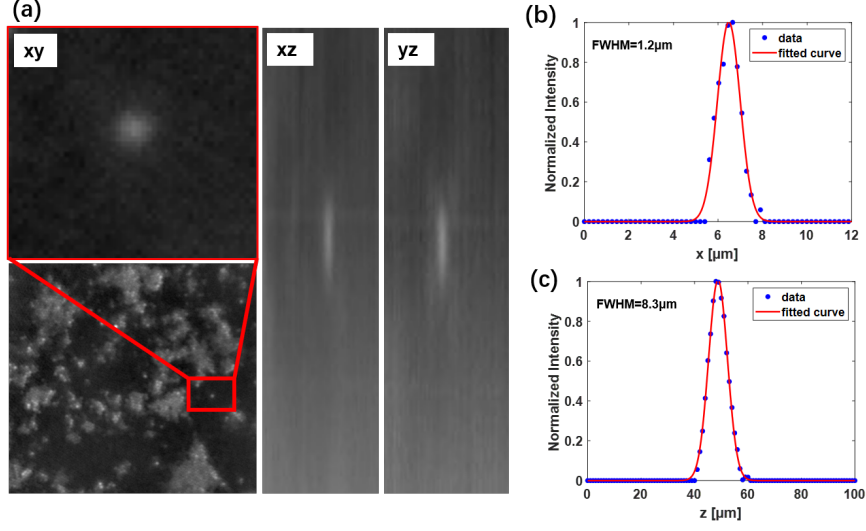


Fig. 3 Measurement of lateral and axial resolution. (a) Images of 700 nm polystyrene beads in three dimensions. The bead labeled with red box is enlarged in the xy plane image. The xz and yz plane images are image stacks taken with a step size of 1 μm axially. (b-c) Measured PSF function along x and z, which reveals the lateral resolution of 1.2 μm and axial resolution of 8.3 μm.

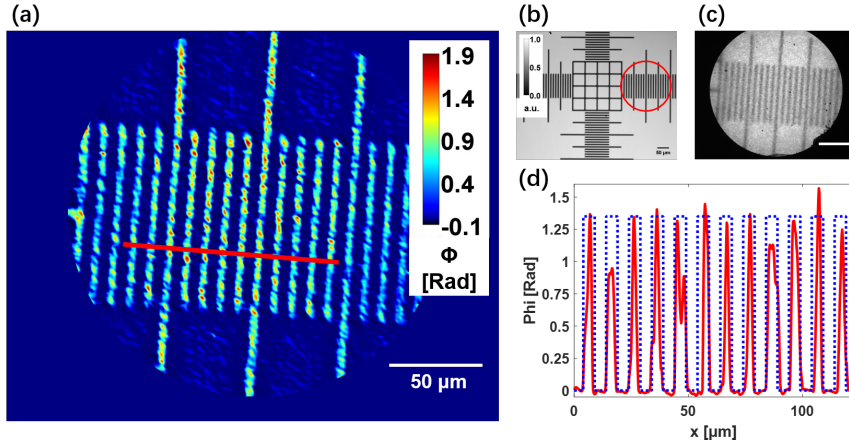


Fig. 4 Measurement of 10 μm calibration slide. (a) The integrated phase map of the sample. (b) Microscope image of the slide for reference. (c) Raw endoscopic image. (d) Difference between the simulated and measured phase of the red line in (a). Scale bars 50 μm.

To calibrate the system, we measure the actual space shift x_0 and y_0 introduced by the diffraction grating on SLM. We use a 10 μm calibrated scale as the standard sample. For image preprocessing, we first remove the honeycomb pattern of the fiber bundle with spatial Gaussian filtering for every raw image, then subtract the filtered background image to get the preprocessed image. The integrated phase map in Fig. 4 (a) can be obtained with preprocessed images by Equation (4) and (5). Figure 4 (b)

displays the microscope image of the slide captured with a 10X objective. The red circle region labels the field of view in endoscopy, and the original endoscopic image is shown in Fig. 4 (c). The phase gradients information and calculation progress in detail can refer to Supplementary Section 2. We calculate the ideal phase of the calibrated scale with $\varphi_0(x, y) = \frac{2\pi}{\lambda} (n - n_0) d$, where $\lambda = 780nm$ is the central wavelength, $n = 1.51$ is the refractive index of the glass, $n_0 = 1$ is the refractive index of the air, $d = 340nm \pm 20nm$ is the height of the sample. The red line section in the phase map (Fig. 4 (a)) is fitted to the ideal phase profile, as is shown in Fig. 4 (d), which offers actual shear distance $x_0 = y_0 = 373nm$. The shear estimation process can refer to Ref.[41].

3.2 Imaging biological specimen

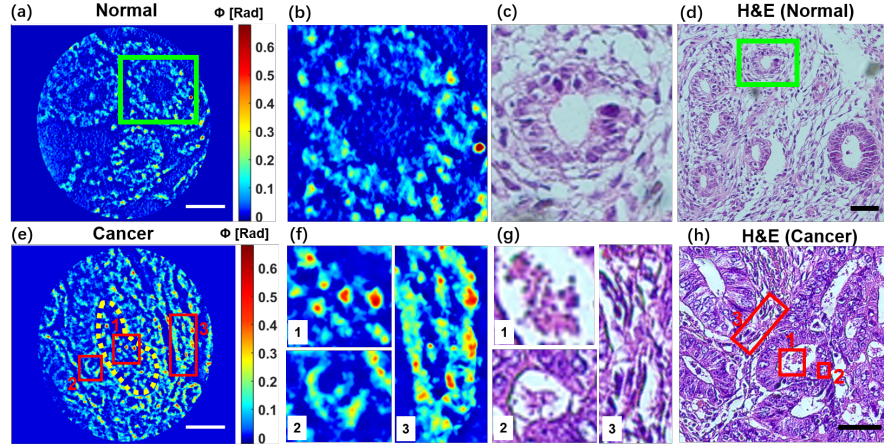


Fig. 5 Measurement of hematoxylin and eosin (H&E) -stained proliferative endometrium (a-d) and grade 2 endometrial adenocarcinoma (e-h). (a,e) Integrated phase maps of the sample, which points out normal circular gland and tumor irregular-shaped gland. (b,c) Enlarged details of the circular gland. (f,g) Enlarged details of secretory, cell and stroma, labeled with 1-3, respectively. (d,h) Microscopic images under 10X objective. Scale bars 50 μm .

In order to evaluate the imaging capability of FGLIM in pathology, Hematoxylin and Eosin (H&E) stained endometrial slides were used as examples. Although the pathologic slices were stained with H&E, they can be considered nearly unlabeled and transparent samples in the NIR-I window [42]. Figures 5 (a-d) show images of proliferative endometrium, where the green box highlights an endometrial gland with regular shape, containing some cell-like materials. Figures 5 (e-h) depict images of grade 2 endometrial adenocarcinoma, where an irregular-shaped endometrial gland is located in the center of the image, indicated by the yellow dotted line. In Fig. 5 (f) and (g), region 1 shows the secretory in the center of the gland, region 2 shows the tumor cell within the gland, and region 3 is the tumor stroma filled among the glands. The FGLIM phase images enable the identification of normal and cancerous endometrial slides with different pathological structures and gland shapes.

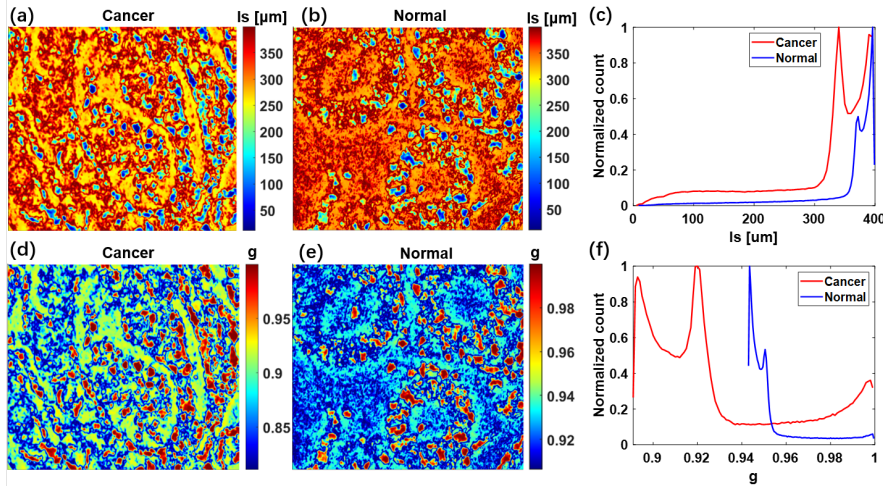


Fig. 6 Scattering properties of endometrial slices in Fig.5; field of view $163\mu\text{m} \times 122\mu\text{m}$. (a,b) Scattering mean free path (ls) maps of the slices. (c) The comparison of the histograms from the ls maps shows that the normal slice has a stronger scattering effect than the cancer slice. (d,e) Anisotropy factor (g) maps of the slices. (f) The comparison of the histograms from the ls maps shows the distinct peak distribution of cancer and normal slices.

To enhance the diagnosis of proliferative endometrium and grade 2 endometrial adenocarcinoma, we have conducted a deeper analysis of the scattering parameters in endometrial tissue slices, specifically focusing on the scattering mean free path (ls) and anisotropy factor (g). The ls represents the average distance between two consecutive scattering events, while the g is the average cosine of the scattering angle. As the tissue slice is $4\mu\text{m}$ thick, we calculate ls and g in a field of view measuring $163\mu\text{m} \times 122\mu\text{m}$ using the scattering-phase theorem and the procedure of calculating g and ls maps can be found in Ref.[43, 44]. Figures 6 (a) and (b) depict the ls maps of endometrial adenocarcinoma and proliferative endometrium, respectively. Analyzing the histograms of these ls maps, we observe that proliferative endometrium exhibits a longer ls than endometrial adenocarcinoma, as illustrated in Fig. 6 (c). This implies that the scattering is stronger in the former. This finding is consistent with the fact that when the tissue slice is placed on white paper, the scattering effect can be more pronounced if the sample is homogeneous because the virtual trans-illumination introduced by the white paper has larger intensity and less energy loss. Figures 6 (d) and (e) display the g maps of endometrial slices. Notably, the variation range of g is larger in endometrial adenocarcinoma than in proliferative endometrium. Moreover, the histogram peaks of the endometrial slices are entirely staggered, as shown in Fig.6 (f). A higher g value signifies that angular scattering is biased more toward the forward direction. Since our system images slice with small optical thickness in reflection geometry, the more inhomogeneous the sample, the stronger the scatter effect introduced by the white paper. The marked differences in ls and g between proliferative endometrium and endometrial adenocarcinoma suggest that our system has the potential to diagnose cancer using scattering parameters.

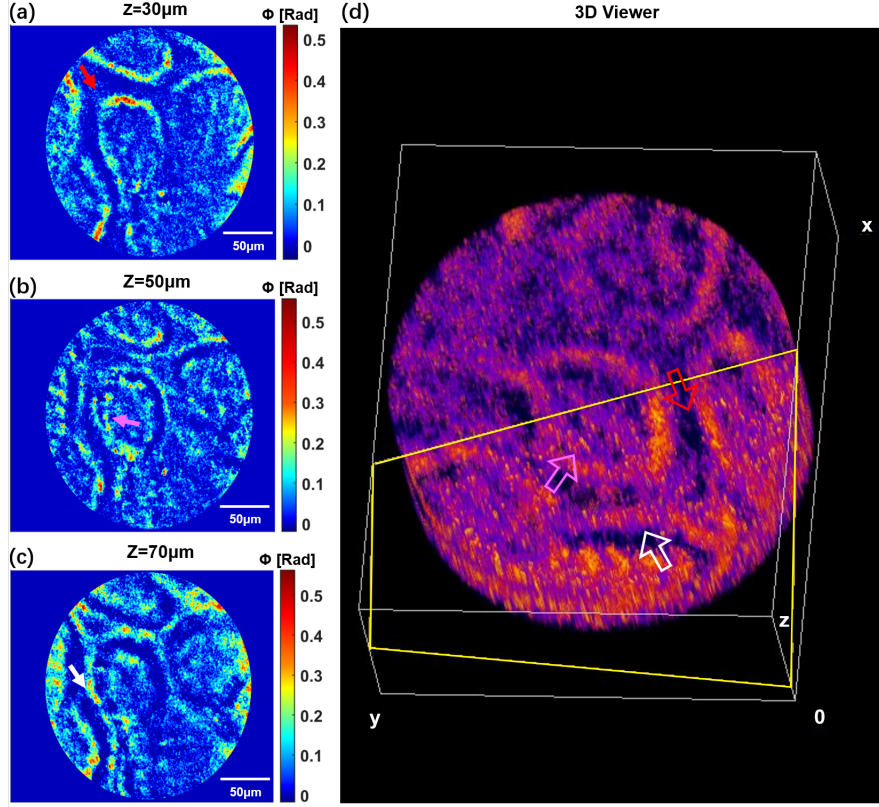


Fig. 7 Measurement on the skin of the streaky pork. (a) Phase at stratum spinosum (SS) layer. (b) Phase at stratum basale-dermis (SB) layer. (c) Phase at dermis (D) layer. (d) The 3D rendering of the phase stack with a size of $250 \times 250 \times 180 \mu\text{m}^3$. The yellow box is a cross-section view. The red arrow denotes canyon in SS layer; The pink arrow points the cell in SB layer; The white arrow shows fibrous components in D layer.

To demonstrate the imaging performance of FGLIM on thick and opaque biological samples, we used a 10 mm thick streaky pork as an example. We performed axial scanning of the sample with a step size of $10 \mu\text{m}$ in the z -direction. The obtained results, as shown in Fig. 7 (a-c), illustrate the phase maps of optical sections at different depths ($30 \mu\text{m}$, $50 \mu\text{m}$, and $70 \mu\text{m}$) within the sample. In Fig. 7 (a), the stratum spinosum layer with canyon-like characteristics is clearly visible, pointed out with a red arrow. In Fig. 7 (b), the canyon becomes less distinct and is filled with the stratum basale layer, and a cell in the dermis is indicated with a pink arrow, representing the stratum basale-dermis layer at a depth of $50 \mu\text{m}$. Figure 7 (c) shows fibrous components labeled by the white arrow at the basis of the stratum papillae, imaged at the depth of $70 \mu\text{m}$. These results highlight the capability of FGLIM to image through thick and turbid samples, revealing textural features at different depths of the layers without the need for stains or fluorescence indicators. Figure 7 (d) presents a 3D view of the tomographic phase stacks, offering a comprehensive view of the layers

from 0 μm to 180 μm . The cross-section in the plane marked by the yellow trapezoid displays phase details marked by arrows corresponding to those shown in Fig. 7 (a-c). This demonstrates the high axial resolution of FGLIM in identifying the layers of the epidermis and dermis with distinct structures.

4 Summary

We have developed FGLIM, a flexible endoscopic QPI system capable of imaging unlabeled thick turbid samples. FGLIM overcomes the limitations of bulk optical setups in traditional QPI microscopes and extends the advantages of QPI to a wider range of applications. With a fiber tip diameter of only 2.5mm, FGLIM can navigate even in narrow nasal sinuses and bronchi, making it an exciting development for endoscopic imaging.

In our system, we perform chessboard gratings in the Fourier domain for high space bandwidth product and accurate modulation with less-cost amplitude type SLM, which verifies the feasibility of wavefront sensing in endoscopic imaging. The wavefront sensing has great potential for the field of QPI endoscopes due to its simple setup: only a grating is needed before the imaging sensor. With state-of-the-art metasurface gratings reported previously [45, 46], the QPI technique could be made compatible with existing endoscopes, opening up possibilities for auxiliary observation within a highly compact system. This technique can help fluorescent endoscopes, optical coherence tomography endoscopes, and electronic endoscopes for fast label-free endogenous contrast imaging, diagnosing with quantitative phase information, and tomographic imaging. We believe that with the improvement of manufacturing accuracy and the maturity of the technology, metasurface gratings might replace SLM to perform ideal wavefront modulation. FGLIM builds the original model and validates the wavefront sensing with gratings for QPI endoscopic systems, which might revolutionize endoscopy for biomedicine.

Our system provides quantitative phase maps with lateral resolution of 1.2 μm , axial resolution of 8.3 μm , and phase sensitivity of 16 nm. The measured resolution can be further improved by developing algorithms to reduce noise and aberration, designing a miniature objective with higher magnification and larger numerical aperture, and using a light source with a broader spectrum. We demonstrate the imaging ability of FGLIM with pathological endometrial slides and 10mm thick unstained mammalian tissue section. FGLIM can identify normal and tumor glands, secretory, canyons, and fibrous components. In addition to morphology, FGLIM shows distinct differences in scattering mean free path and anisotropy factor in the case of pathological endometrial slides. For tomographic imaging, the penetration depth is determined by the working distance of the micro-objective and the transparency of the sample. In the case of 10mm thick unstained streaky pork, the penetration depth can reach up to approximately 180 μm . Through tomographic phase images, FGLIM can identify epidermis and dermis layers with characteristics like canyons, dermis cells, and fibrous tissue. Through these results, FGLIM provides direct morphological and phase information in different depths with nearly microscopic resolution, which might potentially expedite

preoperative diagnosis and reduce the processing time of endoscopic biopsy, routine section sampling, and comprehensive staining for traditional golden standards.

Overall, FGLIM provides a simple solution for wavefront sensing in QPI endoscopic applications. With its small fiber tip, high resolution, good optical sectioning ability, and quantitative phase information, FGLIM has the potential to impact the field of medical imaging and clinical endoscopic diagnostics.

5 Methods

5.1 FGLM System Configuration

The optical setup is shown in Fig. 1. The LED for illumination has a wavelength of 780 nm and a full-width half-maximum of 30 nm, which is coupled into the light guide and illumination fibers. The illumination fibers (Sumita, SOG-120C) with the divergent angle of 120° surround the fiber bundle to create the ring illumination. For image collection, a gradient refractive index (GRIN) lens (GRINTECH, NEM-100-25-10-860-DS, NA=0.5, 2.6X) with an outer diameter of 1mm works as the micro-objective. The working distance of the GRIN lens is about 180 μm in the air and 250 μm in the water. The collected image is then transferred by a 1-m-length fiber bundle (Fujikura, FIGH-30-650S) with 30,000 cores. The average core diameter is 3 μm , and core-to-core spacing is about 3.5 μm . The outer diameter of the fiber bundle is 750 μm , and the imaging diameter is 650 μm . The objective (Olympus UPLXAPO, 10X, 0.4NA) accompanied with the tube lens collect images from the fiber bundle for further phase modulation. As the fiber cores act as sampling pattern with a period of 3.5 μm , the 10X objective has a magnification of 10, which meets the Nyquist sampling condition for the image field with an ideal resolution of 1.2 μm . To modulate the phase of the field, an amplitude type SLM (UPOLabs, HDLSLM80RA, 60 Hz) is used to display chessboard grating. The grating has a period of 2400 pixels on the SLM. A CMOS (Basler, acA1300-60gmNIR, 60Hz) records the interferograms of the differentiated wavefront. The phase reconstruction algorithm is real-time. The phase imaging speed of the system is 2 Hz due to SLM (stabilization time 100ms) and the CMOS and can be improved with a ferroelectric liquid crystal modulator (100 μs response time) and sCMOS for high-speed imaging.

5.2 Monte Carlo Simulation

We utilized PyXOpto, an open source software, to perform Monte Carlo simulation. To simplify the simulation, we only model the left half of the probe cross-section, and replace the annular illumination fiber bundle with a single illumination fiber, and the entire imaging bundle with a single imaging fiber. The detector fiber bundle had a diameter of 650 μm , NA of 0.5, and a refractive index of 1.45, while the illumination fiber bundle had a diameter of 250 μm , NA of 0.9, and a refractive index of 1.45. The distance between the two fiber cores was set to 875 μm . To visualize the path of photon packets through the sample, we used a tool called sampling volume, which summed the photon packet weights along the y-axis.

5.3 Sample Preparation and Imaging

5.3.1 700nm polystyrene beads preparation

The polystyrene beads (LMNANO, 700 nm, 50 mg/ml, coefficient of variation $\leq 3.0\%$) are diluted with water to get dispersed particles. A dilution of 700nm beads was placed on the glass slide for air drying. The dried beads are stuck on the glass slide and can be observed with the endoscopy directly.

5.3.2 Histological slides

Hematoxylin and Eosin (H&E) stained endometrial slides were kindly provided by Fifth Hospital in Wuhan. To exclude environmental light, the experiments were carried out in a dark room, and a colored glass filter was placed before the CMOS to block light with wavelengths below 695 nm. The illumination central wavelength is 780 nm, which falls within the near-infrared (NIR) window called NIR-I. NIR-I is defined as the biological transparency window for imaging. Thus, the slides can be considered as transparent sample in our case.

5.3.3 Streaky pork preparation

The streaky pork was washed with phosphate buffered saline (PBS, Biosharp) and soaked in 4 % paraformaldehyde (Biosharp) for one day at room temperature. Then, the fixed sample was washed with PBS and placed whole on a glass slide for imaging. The axial scanning step size is 10 μm .

List of Supplemental Materials. 1. Supplementary Information

Data availability. The data that support the findings of this study are available from the corresponding author upon reasonable request.

Code availability. The MATLAB code used for phase reconstruction is available from the corresponding authors upon reasonable request.

Acknowledgements. This work is supported by National Natural Science Foundation of China (52275533); National Key R&D Plan International Cooperation Key Special Project (2022YFE0128800) and Shenzhen Technical Project (JCY J20210324141814038). The authors would like to thank Dr. Yanli Ouyang from Fifth Hospital in Wuhan for providing histological slices.

Author contributions. J.W. proposed the idea, constructed the instrument, wrote the algorithm, performed imaging, and analyzed the data. J.W. and C.H. wrote the paper, processed data, and draw figures. W.Y. and Y.J gave support on instrument setup. Y.Z. provided biospecimen analysis. X.L., X.J. and W.L. supervised the work.

Declarations

The authors declare no conflicts of interest.

References

- [1] Mannath, J., Ragunath, K.: Role of endoscopy in early oesophageal cancer. *Nature Reviews Gastroenterology & Hepatology* **13**(12), 720–730 (2016) <https://doi.org/10.1038/nrgastro.2016.148>
- [2] Li, J., Ebendorff-Heidepriem, H., Gibson, B.C., Greentree, A.D., Hutchinson, M.R., Jia, P., Kostecki, R., Liu, G., Orth, A., Ploschner, M., Schartner, E.P., Warren-Smith, S.C., Zhang, K., Tsiminis, G., Goldys, E.M.: Perspective: Biomedical sensing and imaging with optical fibers—Innovation through convergence of science disciplines. *APL Photonics* **3**(10), 100902 (2018) <https://doi.org/10.1063/1.5040861>
- [3] Kurniawan, N., Keuchel, M.: Flexible gastro-intestinal endoscopy — clinical challenges and technical achievements. *Computational and Structural Biotechnology Journal* **15**, 168–179 (2017) <https://doi.org/10.1016/j.csbj.2017.01.004>
- [4] Klioutchnikov, A., Wallace, D.J., Frosz, M.H., Zeltner, R., Sawinski, J., Pawlak, V., Voit, K.-M., Russell, P.S.J., Kerr, J.N.D.: Three-photon head-mounted microscope for imaging deep cortical layers in freely moving rats. *Nature Methods* **17**(5), 509–513 (2020) <https://doi.org/10.1038/s41592-020-0817-9>
- [5] Kučikas, V., Werner, M.P., Schmitz-Rode, T., Louradour, F., van Zandvoort, M.A.M.J.: Two-Photon Endoscopy: State of the Art and Perspectives. *Molecular Imaging and Biology* (2021) <https://doi.org/10.1007/s11307-021-01665-2>
- [6] Loterie, D., Goorden, S.A., Psaltis, D., Moser, C.: Confocal microscopy through a multimode fiber using optical correlation. *Optics Letters* **40**(24), 5754 (2015) <https://doi.org/10.1364/OL.40.005754>
- [7] Zhang, H., Vyas, K., Yang, G.-Z.: Line scanning, fiber bundle fluorescence HiLo endomicroscopy with confocal slit detection. *Journal of Biomedical Optics* **24**(11), 1 (2019) <https://doi.org/10.1117/1.JBO.24.11.116501>
- [8] Li, J., Thiele, S., Quirk, B.C., Kirk, R.W., Verjans, J.W., Akers, E., Bursill, C.A., Nicholls, S.J., Herkommer, A.M., Giessen, H., McLaughlin, R.A.: Ultrathin monolithic 3D printed optical coherence tomography endoscopy for preclinical and clinical use. *Light: Science & Applications* **9**(1), 124 (2020) <https://doi.org/10.1038/s41377-020-00365-w>
- [9] Gora, M.J., Suter, M.J., Tearney, G.J., Li, X.: Endoscopic optical coherence tomography: Technologies and clinical applications [Invited]. *Biomedical Optics Express* **8**(5), 2405 (2017) <https://doi.org/10.1364/BOE.8.002405>
- [10] Park, Y., Depeursinge, C., Popescu, G.: Quantitative phase imaging in biomedicine. *Nature photonics* **12**(10), 578–589 (2018) <https://doi.org/10.1038/s41566-018-0253-x>

- [11] Micó, V., Zheng, J., Garcia, J., Zalevsky, Z., Gao, P.: Resolution enhancement in quantitative phase microscopy. *Advances in Optics and Photonics* **11**(1), 135 (2019) <https://doi.org/10.1364/AOP.11.000135>
- [12] Hu, C., He, S., Lee, Y.J., He, Y., Kong, E.M., Li, H., Anastasio, M.A., Popescu, G.: Live-dead assay on unlabeled cells using phase imaging with computational specificity. *Nature communications* **13**(1), 1–8 (2022) <https://doi.org/10.1038/s41467-022-28214-x>
- [13] Kim, G., Ahn, D., Kang, M., Park, J., Ryu, D., Jo, Y., Song, J., Ryu, J.S., Choi, G., Chung, H.J., *et al.*: Rapid species identification of pathogenic bacteria from a minute quantity exploiting three-dimensional quantitative phase imaging and artificial neural network. *Light: Science & Applications* **11**(1), 1–12 (2022) <https://doi.org/10.1038/s41377-022-00881-x>
- [14] Cacace, T., Bianco, V., Ferraro, P.: Quantitative phase imaging trends in biomedical applications. *Optics and Lasers in Engineering* **135**, 106188 (2020) <https://doi.org/10.1016/j.optlaseng.2020.106188>
- [15] Roitshtain, D., Wolbromsky, L., Bal, E., Greenspan, H., Satterwhite, L.L., Shaked, N.T.: Quantitative phase microscopy spatial signatures of cancer cells. *Cytometry Part A* **91**(5), 482–493 (2017) <https://doi.org/10.1002/cyto.a.23100>
- [16] Singh, V.R., Yang, Y.A., Yu, H., Kamm, R.D., Yaqoob, Z., So, P.T.C.: Studying nucleic envelope and plasma membrane mechanics of eukaryotic cells using confocal reflectance interferometric microscopy. *Nat Commun* **10**(1), 3652 (2019) <https://doi.org/10.1038/s41467-019-11645-4>
- [17] Choi, Y., Hosseini, P., Kang, J.W., Kang, S., Yang, T.D., Hyeon, M.G., Kim, B.-M., So, P.T.C., Yaqoob, Z.: Reflection phase microscopy using spatio-temporal coherence of light. *Optica* **5**(11), 1468 (2018) <https://doi.org/10.1364/OPTICA.5.001468>
- [18] Zhou, R., Jin, D., Hosseini, P., Singh, V.R., Kim, Y.-h., Kuang, C., Dasari, R.R., Yaqoob, Z., So, P.T.C.: Modeling the depth-sectioning effect in reflection-mode dynamic speckle-field interferometric microscopy. *Opt. Express* **25**(1), 130 (2017) <https://doi.org/10.1364/OE.25.000130>
- [19] Kandel, M.E., Hu, C., Naseri Kouzehgarani, G., Min, E., Sullivan, K.M., Kong, H., Li, J.M., Robson, D.N., Gillette, M.U., Best-Popescu, C., Popescu, G.: Epi-illumination gradient light interference microscopy for imaging opaque structures. *Nature communications* **10**(1), 4691 (2019) <https://doi.org/10.1038/s41467-019-12634-3>
- [20] Hu, C., Zhu, S., Gao, L., Popescu, G.: Endoscopic diffraction phase microscopy. *Opt. Lett.* **43**(14), 3373 (2018) <https://doi.org/10.1364/OL.43.003373>

- [21] Sun, J., Wu, J., Wu, S., Goswami, R., Girardo, S., Cao, L., Guck, J., Koukourakis, N., Czarske, J.W.: Quantitative phase imaging through an ultra-thin lensless fiber endoscope. *Light: Science & Applications* **11**(1), 1–10 (2022) <https://doi.org/10.1038/s41377-022-00898-2>
- [22] Badt, N., Katz, O.: Label-free video-rate micro-endoscopy through flexible fibers via fiber bundle distal holography (FiDHo). In: *OSA Imaging and Applied Optics Congress 2021* (3D, COSI, DH, ISA, pcAOP), pp. 4–4. Optica Publishing Group, ??? (2021). <https://doi.org/10.1364/DH.2021.DW4C.4>
- [23] Choi, W., Kang, M., Hong, J.H., Katz, O., Lee, B., Kim, G.H., Choi, Y.: Flexible-type ultrathin holographic endoscope for microscopic imaging of unstained biological tissues. *Nature Communications* **13**, 4469 (2022) <https://doi.org/10.1038/s41467-022-32114-5>
- [24] Ford, T.N., Chu, K.K., Mertz, J.: Phase-gradient microscopy in thick tissue with oblique back-illumination. *Nature Methods* **9**(12), 1195–1197 (2012) <https://doi.org/10.1038/nmeth.2219>
- [25] Ando, Y., Koida, K., Sawahata, H., Sakurai, T., Natsume, M., Kawano, T., Numano, R.: Reflectance imaging by fiber bundle endoscope: Vertical reconstruction by multipositional illumination. *AIP Conference Proceedings* **1709**(1), 020009 (2016) <https://doi.org/10.1063/1.4941208>
- [26] Costa, P.C., Guang, Z., Ledwig, P., Zhang, Z., Neill, S., Olson, J.J., Robles, F.E.: Towards in-vivo label-free detection of brain tumor margins with epi-illumination tomographic quantitative phase imaging. *Biomed. Opt. Express* **12**(3), 1621 (2021) <https://doi.org/10.1364/BOE.416731>
- [27] Wang, Y., Kandel, M.E., Fanous, M.J., Hu, C., Chen, H., Lu, X., Popescu, G.: Harmonically decoupled gradient light interference microscopy (HD-GLIM). *Opt. Lett.* **45**(6), 1487 (2020) <https://doi.org/10.1364/OL.379732>
- [28] McIntyre, T.J., Maurer, C., Fassel, S., Khan, S., Bernet, S., Ritsch-Marte, M.: Quantitative SLM-based differential interference contrast imaging. *Opt. Express* **18**(13), 14063 (2010) <https://doi.org/10.1364/OE.18.014063>
- [29] Naglič, P., Pernuš, F., Likar, B., Bürmen, M.: Lookup table-based sampling of the phase function for monte carlo simulations of light propagation in turbid media. *Biomed. Opt. Express* **8**(3), 1895–1910 (2017) <https://doi.org/10.1364/BOE.8.001895>
- [30] Naglič, P., Pernuš, F., Likar, B., Bürmen, M.: Limitations of the commonly used simplified laterally uniform optical fiber probe-tissue interface in monte carlo simulations of diffuse reflectance. *Biomed. Opt. Express* **6**(10), 3973–3988 (2015) <https://doi.org/10.1364/BOE.6.003973>

- [31] Naglič, P., Zelinskyi, Y., Pernuš, F., Likar, B., Bürmen, M.: pyxopto: An open-source python library with utilities for fast light propagation modeling in turbid media. In: Diffuse Optical Spectroscopy and Imaging VIII, vol. 11920, p. 1192012. SPIE, ??? (2021). <https://doi.org/10.1117/12.2615340> . International Society for Optics and Photonics
- [32] Cheong, W.F., Prah, S.A., Welch, A.J.: A review of the optical properties of biological tissues. IEEE Journal of Quantum Electronics **26**(12), 2166–2185 (1990) <https://doi.org/10.1109/3.64354>
- [33] Ding, H., Wang, F., Lin, F., Wang, G., Li, W., Lichty, W.: Analysis of the sensitivity of reflectance near-infrared tissue oximeter using the methods of simulation and experiment. In: 1999 International Conference on Biomedical Optics, vol. 3863, pp. 59–65 (1999). <https://doi.org/10.1117/12.364365> . SPIE
- [34] Perperidis, A., Parker, H.E., Karam-Eldaly, A., Altmann, Y., Dhaliwal, K., Thomson, R.R., Tanner, M.G., McLaughlin, S.: Characterization and modelling of inter-core coupling in coherent fiber bundles. Opt. Express **25**(10), 11932 (2017) <https://doi.org/10.1364/OE.25.011932>
- [35] Perperidis, A., Dhaliwal, K., McLaughlin, S., Vercauteren, T.: Image computing for fibre-bundle endomicroscopy: A review. Medical image analysis **62**, 101620 (2020) <https://doi.org/10.1016/j.media.2019.101620>
- [36] Li, S., Saunders, C., Lum, D.J., Murray-Bruce, J., Goyal, V.K., Čížmár, T., Phillips, D.B.: Compressively sampling the optical transmission matrix of a multimode fibre. Light: Science & Applications **10**(1), 1–15 (2021) <https://doi.org/10.1038/s41377-021-00514-9>
- [37] Gordon, G.S., Joseph, J., Alcolea, M.P., Sawyer, T., Williams, C., Fitzpatrick, C.R., Jones, P.H., Di Pietro, M., Fitzgerald, R.C., Wilkinson, T.D., *et al.*: Quantitative phase and polarization imaging through an optical fiber applied to detection of early esophageal tumorigenesis. Journal of Biomedical Optics **24**(12), 126004 (2019) <https://doi.org/10.1117/1.JBO.24.12.126004>
- [38] Eldaly, A.K., Altmann, Y., Perperidis, A., Krstajic, N., Choudhary, T.R., Dhaliwal, K., McLaughlin, S.: Deconvolution and Restoration of Optical Endomicroscopy Images. IEEE Trans. Comput. Imaging **4**(2), 194–205 (2018) <https://doi.org/10.1109/TCI.2018.2811939>
- [39] Choi, I., Lee, K., Park, Y.: Compensation of aberration in quantitative phase imaging using lateral shifting and spiral phase integration. Opt. Express **25**(24), 30771 (2017) <https://doi.org/10.1364/OE.25.030771>
- [40] Nie, Y., Zhou, R.: Beating temporal phase sensitivity limit in off-axis interferometry based quantitative phase microscopy. APL Photonics **6**(1), 011302 (2021) <https://doi.org/10.1063/5.0034515>

- [41] Nguyen, T.H., Kandel, M.E., Rubessa, M., Wheeler, M.B., Popescu, G.: Gradient light interference microscopy for 3D imaging of unlabeled specimens. *Nature communications* **8**(1), 210 (2017) <https://doi.org/10.1038/s41467-017-00190-7>
- [42] Hong, G., Antaris, A.L., Dai, H.: Near-infrared fluorophores for biomedical imaging. *Nat Biomed Eng* **1**(1), 0010 (2017) <https://doi.org/10.1038/s41551-016-0010>
- [43] Wang, Z., Ding, H., Popescu, G.: Scattering-phase theorem. *Opt. Lett.* **36**(7), 1215 (2011) <https://doi.org/10.1364/OL.36.001215>
- [44] Wang, Z., Popescu, G., Tangella, K.V., Balla, A.: Tissue refractive index as marker of disease. *J. Biomed. Opt.* **16**(11), 1 (2011) <https://doi.org/10.1117/1.3656732>
- [45] Kwon, H., Arbabi, E., Kamali, S.M., Faraji-Dana, M., Faraon, A.: Single-shot quantitative phase gradient microscopy using a system of multifunctional metasurfaces. *Nat. Photonics* **14**(2), 109–114 (2020) <https://doi.org/10.1038/s41566-019-0536-x>
- [46] Zhong, H., Wang, Y.: Quantum dots on demand. *Nat. Photonics* **14**(2), 65–66 (2020) <https://doi.org/10.1038/s41566-019-0579-z>